ESKİŞEHİR TECHNICAL UNIVERSITY JOURNAL OF SCIENCE AND TECHNOLOGY
A- APPLIED SCIENCES AND ENGINEERING

19th National Clay Symposium (Clay'2023) Sprecial Issue 2023

`2023, Vol.24, pp. 63-89, DOI:10.18038/estubtda.1370311`

KAOLIN FORMATION IN YATAĞAN (MUĞLA) LIGNITE DEPOSIT

Zeynep BÜÇKÜN *, **Mümtaz ÇOLAK**

Department of Geological Engineering, Faculty of Engineering, Dokuz Eylül University, İzmir, Türkiye

ABSTRACT

The 30-km-long and 10-km-wide, coal-bearing Yatağan Basin is located in SW Anatolia, close to the eastern coast of the Aegean Sea, Türkiye. The basement consists of Menderes Massif metamorphics in the NW part of this intermontane basin, c. 80-km2-large area (Turgut lignite deposit). The Neogene and Quaternary sedimentary filling comprises fluvioterrestrial, limnic and telmatic sediments which contain a mineable coal seam up to 15 m thick, unconformably overlain the basement. Two fresh and six weathered samples were picked up from the Menderes Massif gneiss outcrops of the catchment area. Eight sedimentary rocks, inorganics over and underlying the coal seam, were obtained from four borehole cores. All samples were examined under the optical microscope; XRD, SEM-EDX and ICP-MS analyses were later performed. This study aims to examine the mineralogical content and geochemical processes of the sedimentary rocks from different formations, namely Sekköy and Turgut Formations, which are over- and underlying the lignite horizon, to assess the clay mineral formations and transformations. Gneiss samples contain mainly quartz, plagioclase, K-feldspar, muscovite and biotite with a lesser amount of tourmaline, chlorite, garnet, apatite, zoisite, zircon and Fe-oxides. The -2 µm fraction consists mainly of illite, with fewer smectite and kaolinite. Sericitizitation of feldspar is the main product in gneisses. Coal over-and underlying sedimentary rock samples contain mainly quartz, plagioclase, K-feldspar, muscovite, and biotite with less pyrite and iron oxides. The -2 µm fraction of the sedimentary rock samples consists of variable clay mineral contents. Kaolin content is higher in acidic conditions with an opposite correlation to smectite occurrences. The geochemistry of Menderes Massif gneisses shows that it gave felsic material to the catchment area, whereas the geochemistry of sedimentary rocks is not coherent in all cases. Geochemical parameters like CIA and PIA proved that weathering processes of the source materials prevailed during the generation of these sedimentary units.

Keywords: Turgut, Sekköy, Illite, Smectite, Kaolinisation

1. INTRODUCTION

Since Neogene times Western Anatolia experienced intercontinental tectonics, which formed NW-SE, NE-SW, and E-W trending basins [1-14]. The NW-SE trending Yatağan Basin is one of them being located in SW Anatolia, close to the eastern coast of the Aegean Sea, Türkiye. The 30 km long and 10 km wide basin is filled with Cenozoic siliciclastic and carbonate deposits [15-19]. In the NW part of Yatağan Basin, the Turgut lignite deposit is hosted, occupying a c. 80-km^2-large area; it contains a mineable coal seam up to 15 m thick. Lignite deposits are studied widely and extensively in the region regarding abundance, operability and priority of supply [20-23]. Feldspar, quartz and marble open-pit mines exist in the surrounding area as well. Moreover, the existence of the antique city Stratonikea in the south of Turgut area points to the economic importance of the region in the past, even in the 3rd century BC (Figure 1).

The economic clay potential is yet to be extensively investigated and interpreted in the study area. In addition, there is no study in the literature in which the clay minerals of these sediments are evaluated in detail in the light of mineralogical and geochemical data, field-wide (horizontal) and depth-dependent (vertical) and correlated with other existing findings. The present study focuses on the petrographic, mineralogical and geochemical compositions of the sedimentary rocks over- and underlying the coal seam. The aim is to research the clay mineral formations and to assess the existence of kaolinisation.

---

*Corresponding Author: zeynep.buckun@deu.edu.tr
Received: 02.10.2023 Published: 29.11.2023

2. GEOLOGICAL SETTING

The basement consists of Menderes Massif metamorphic rocks. The stratigraphy of the Menderes Massif is divided into two units consisting of the Late Neoproterozoic Pan-African basement and the Paleozoic-Early Tertiary cover series. In the study area, the observed units belonging to the Menderes Massif Pan-African basement are schist and orthogneiss. The units belonging to the Menderes Massif cover series are phyllite, quartzite, marble alternations succession and overlying platform type and pelagic marbles, respectively. The primary contact between these two series is a regional-scale Pan-African unconformity that defines a deep erosion [24-30].

The Miocene sequence, which unconformably overlays the basement, comprises three formations, namely those of Turgut, Sekköy and Yatağan Formations [18, 19, 31-35]. From bottom to top, Turgut Fm includes conglomerate, sandstone, mudstone, limestone, coal, mudstone deposited under alluvial fan, fluvial and lacustrine conditions, whereas Sekköy Fm comprises coal, silty claystone, mudstone, marl and limestone deposited under telmatic/lacustrine conditions. These formations are conformably overlain by the Yatağan Fm, which hosts conglomerate, sandstone, limestone-marl-mudstone deposited under alluvial fan and lacustrine conditions. Quaternary alluvial deposits constitute the Yatağan Fm (Figures 1, 2).

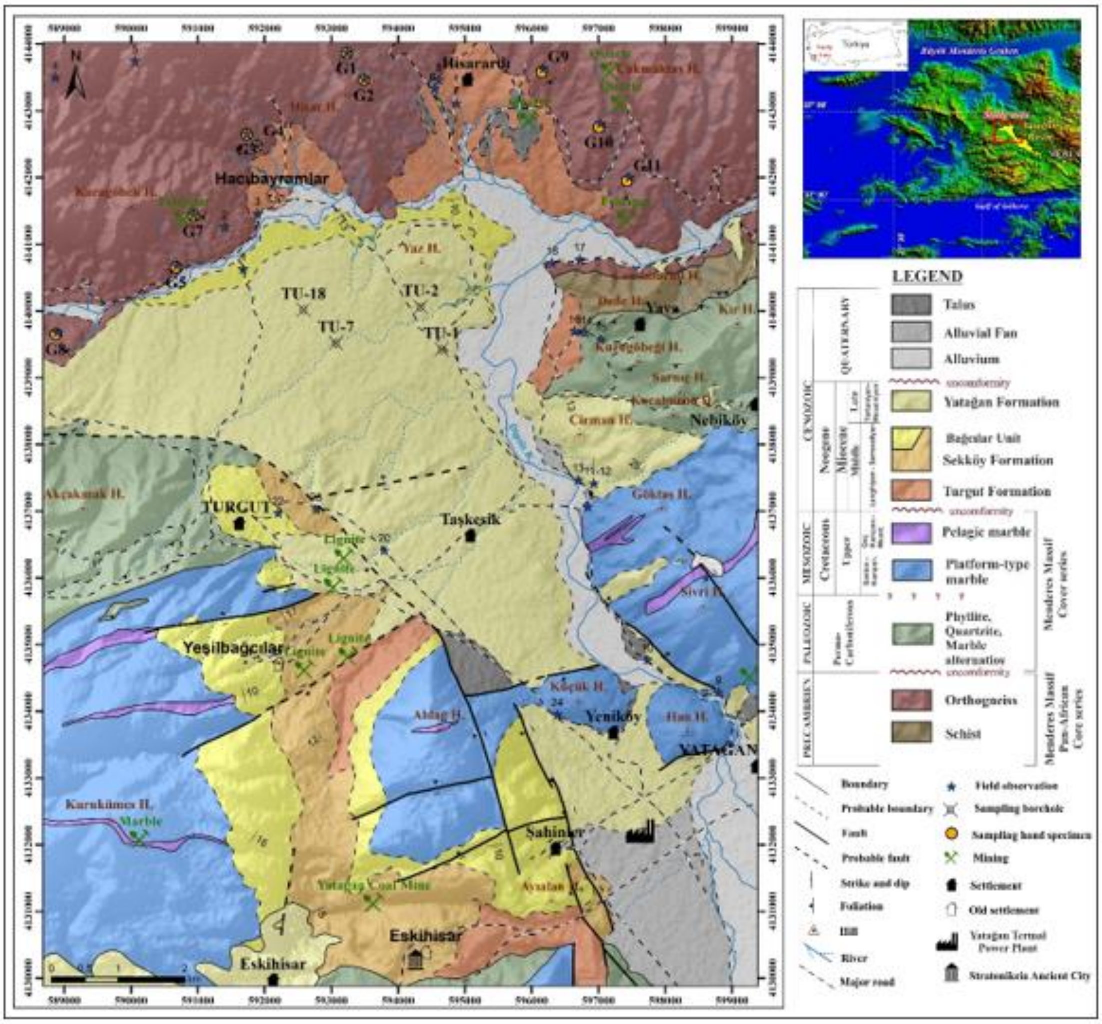

Figure 1. Geological map of Turgut area in Yatağan lignite deposit [18, 27-30].

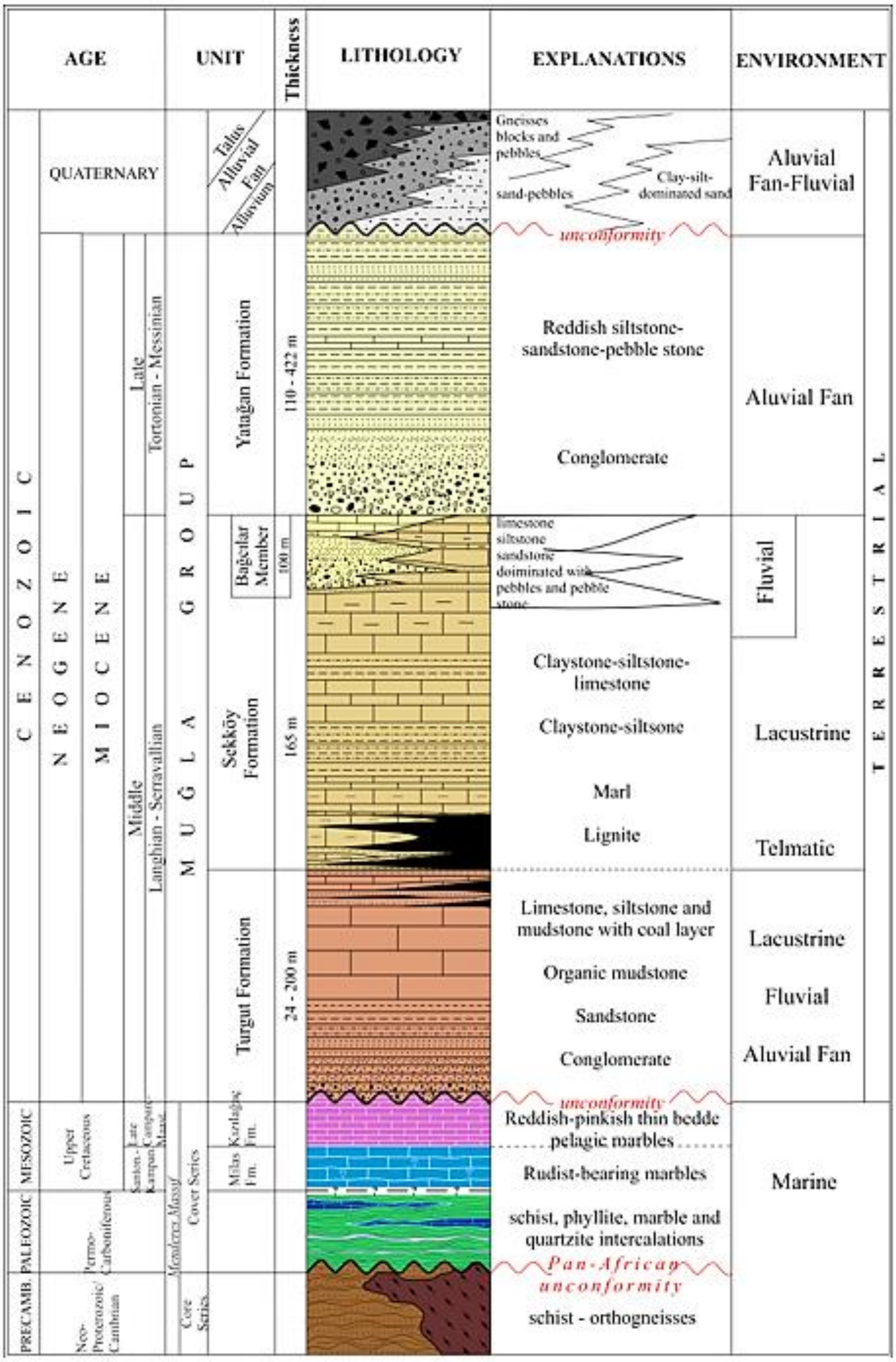

Figure 2. Stratigraphic column of Turgut area in Yatağan Basin [18, 19, 27-30].

3. MATERIALS AND METHODS

Based on field work the geological maps of previous studies [18, 27-30] were revised on a scale of 1:25,000. The geological map was digitised using UTM (Universal Transverse Mercator) projection type, WGS 1984 Datum and Zone: 35 in the ArcGIS™ software ArcMap 10.5 application. NASA Earthdata and 30-m resolution elevation data from the Shuttle Radar Topography Mission (SRTM) were used for the digital elevation model (DEM) [36, 37].

Two fresh,(G1, G5), eight weathered gneiss samples were collected from outcrops in the north margins of the study basin (Figure 1, 3). Eight sedimentary rock samples were obtained from four borehole cores, namely TU-1, TU-2, TU-7 and TU-18; the samples picked up from the coal-overlying layers received the code A and these from the underlying ones B (Figure 1, 4).

Figure 3. Outcrops of the Menderes Massif, Hisar Hill (see Figure 1).

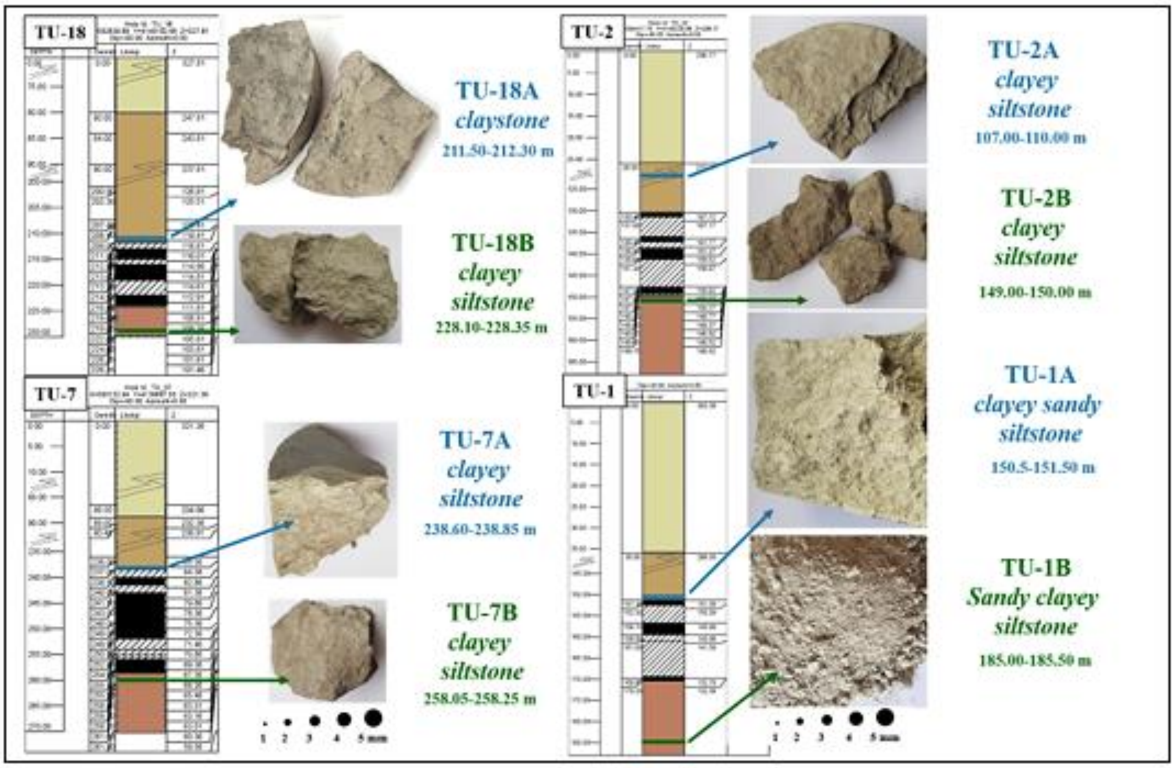

Figure 4. Borehole graphics and the sampled sedimentary rocks.

The gneiss samples were cut perpendicularly to the foliation and examined under the Leica DM750P polarized microscope. The sedimentary rock samples (fraction size > 63 µm) were examined for transformations also under the microscope. The studies were performed at the Department of Geological Engineering, Dokuz Eylül University (İzmir, Türkiye) and the photomicrographs were taken via the Leica DFC 290 HD attachment.

The XRD analysis was carried out on random oriented samples using a Rigaku MiniFlex 600 diffractometer at the Department of Geological Engineering, Dokuz Eylül University (İzmir, Türkiye) using CuKα radiation (k=1.542 Å). The diffractograms were obtained at 33 kV and 15 mA, scanning 2-65° of 2θ with a step size of 2°/min. The clay mineralogical composition was determined after separating the < 2 µm fraction in distilled water by centrifugation. The clay particles were dispersed through ultrasonic vibration for ~15 min. The clay fractions were vacuumed by pipette of the clay suspension and transferred to three glass slides to get oriented preparations. Three different XRD patterns were obtained from three different phases (air-dried, solvated with ethylene glycol at 60°C, and heated at 550°C for 2 h) of each sample at scanning 2-40° of 2θ. Semi-quantitative determinations were obtained by multiplying the intensities of the principal basal reflections of each clay mineral by appropriate factors. The analysing error is 5 wt.% [38]. The crystalline phase identification was carried out using the PDXL2 software package (Rigaku).

Andreasen pipette method was applied to sedimentary rock samples to quantify the < 2 µm fraction of each sample. Each sample was placed in distilled water to get a suspension. In order to prevent the suspended grains from coagulating and flocculating in the liquid, the pH of the suspension was increased by using NH_3, and in order to ensure that the grains were well dispersed in the liquid, the suspension was kept in an ultrasonic bath and mixed in an automatic shaker. The suspension was placed into an Andreasen pipette vessel, a narrow and high cylindrical glass container with a sedimentation column height of 200 mm, which has a 10 ml chamber sealed with glass stopper on the top and designed to draw samples from the bottom. Then the vessel was shaken vigorously and placed on a stable plane. The temperature of the pulp was kept constant at 23°C during the experiment; the pulp was drawn into the 10 ml chamber and taken out of the Andreasen pipette into a weighed beaker at specified time intervals, and the remaining body after evaporation was weighed again. Calculations were made based on Stoke's law and the clay grain size (< 2 µm) content of the sample was calculated according to the DIN 66115 standard [39].

Electron microscope examinations were undertaken on gold-coated gneiss and sedimentary rock samples (particle size > 63 µm) using a Carl Zeiss 300VP Scanning Electron Microscope (SEM) at Central Research Laboratories Research and Application Center (İKÇÜ-MERLAB), Katip Çelebi University (İzmir, Türkiye).

Whole rock chemical analyses were performed using an Inductively Coupled Plasma-Mass Spectrometer (ICP-MS) following a lithium borate fusion and dilute acid digestion of a 0.2 g sample in ACME Analytical Laboratories, Canada.

Abbreviations of the minerals and associated phases in the figures and tables follow the literature, which are listed in Table 1 [40, 41].

Table 1. List of the abbreviations of the minerals and associated phases [40, 41].

Symbol	Mineral Name	IMA status*	Symbol	Mineral Name	IMA status*
Afs	alkali feldspar	GROUP	Jd	jadeite	A
Alp	allophane	G	Kfs	K-feldspar	informal
An	anorthite	GROUP	Kn	kaolin	Group
Ap	apatite	GROUP	Kln	kaolinite	A
Bt	biotite	GROUP	Mca	mica	GROUP
Chl	chlorite	GROUP	Mnt	montmorillonite	G
Cpx	clinopyroxene	GROUP	Ms	muscovite	A
Di	diopside	G	Opq	opaque mineral	informal
Fsp	feldspar	GROUP	Pl	plagioclase	GROUP
Gbs	gibbsite	A	Py	pyrite	G
Grt	garnet	GROUP	Qz	quartz	A
Gp	gypsum	G	Ser	sericite	D
Hem	hematite	A	Sme	smectite	GROUP
Hly	halloysite	G	Tur	tourmaline	GROUP
Hbl	hornblende	GROUP	Zr	zircon	G
Ilt	illite	GROUP	Zo	zoisite	G
Others					
IO	*Iron oxides*				
ML	*Mixed-layer phases*				

* International Mineralogical Association (IMA) abbreviations: A = Approved; D = Discredited; G = Grandfathered (generally regarded as valid mineral name); GROUP = Name designates a group of mineral species.

4. RESULTS AND DISCUSSION

4.1. Petrographical and Mineralogical Investigations

The gneiss of the study area has porphyroblastic texture. The microscopic composition of these samples consists mainly of quartz, plagioclase, K-feldspar, muscovite, and biotite. Sericizitation of the feldspars is widespread, while argillization of K-feldspar is less (Figure 5 (a-d)). Chloritization of biotite is rare and chlorite comprises fibrous bundles (Figure 5 (e, f)). Garnet and turmaline minerals are relatively abundant to apatite, zircon and zoisite (Figure 5 (g-j)).

Major mineral composition of the gneiss samples as detected by XRD analysis are quartz, plagioclase, K-feldspar and mica minerals (Figure 6 (a)) and the relative abundances of these minerals are given in Table 2. Illite is the main clay mineral, while smectite and kaolinite determined in -2 µm fraction of the samples (Figure 6 (b)) and the semi-quantitative results of these clay minerals are given in Table 3.

SEM results show that the main transformation is sericizitation (Figure 7). Smectite formations from opal-CT is shown in Figure 7 (b). Rosette chlorite was determined in the gneiss samples showing the formation of chlorite from biotite. (Figure 8).

In many studies, orthogneisses, which are defined as "augen" or "granitic", have been named in various ways such as to describe the degree of metamorphism (sillimanite gneiss), deformation characteristics (mylonitic gneiss) and the rock of origin (orthogneiss) as well. Additionally, these intrusions are categorized into three groups based on their mineral compositions and classified based on the type and content of mafic minerals in the rock biotite orthogneiss, amphibole orthogneiss and tourmaline leucocratic orthogneiss [42, 43]. Based on their primary textures and mineral compositions, studied samples are biotite orthogneisses which are the most abundant type in the study area.

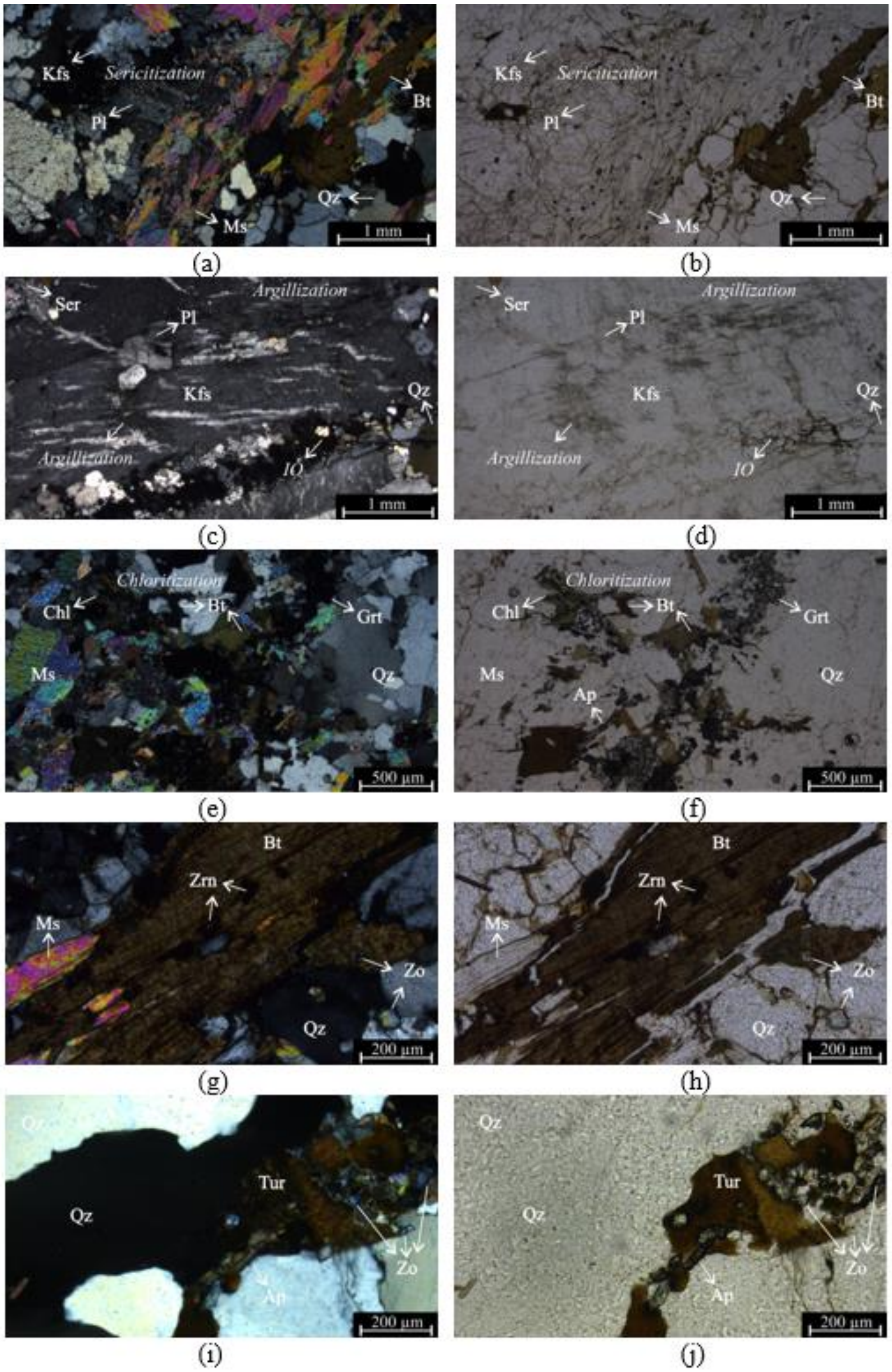

Figure 5. Photomicrographs of the gneiss samples: (a) with crossed polarizers. Sericitization of K-feldspar and plagioclase; (b) in plane polarized light (G9); (c) with crossed polarizers. Sericitization and argillization of feldspar minerals. Pertitic texture of K-feldspar; (d) in plane polarized light (G4); (e) with crossed polarizers. Chloritization of biotite; (f) in plane polarized light (G1); (g) with crossed polarizers. Zircon inclusions in biotite; (h) in plane polarized light (G2); (i) with crossed polarizers. Tourmaline, apatite and zoisite minerals; (j) in plane polarized light (G1).

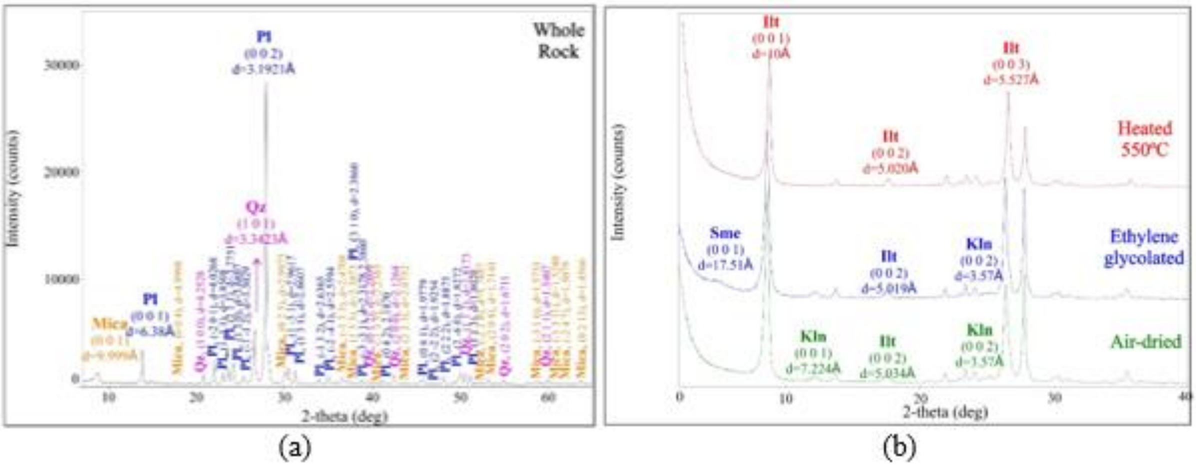

Figure 6. X-Ray diffractograms of (a) whole rock mineral compositions; (b) clay compositions of -2 μm fraction of G8 as a representative gneiss sample.

Table 2. Relative abundance* of minerals in the analysed gneiss samples.

	G1	G2	G3	G4	G5	G7	G8	G9	G10	G11
Qz	va	va	va	va	va	va	s	va	va	va
Pl	m	m	m	a	a	a	va	m	a	va
Kfs	vs	?	vs	vs	s	vs	?	?	vs	vs
Mica	s	s	s	m	m	s	vs	s	m	s

* va: very abundant, a: abundant, m: moderate, s: scarce, vs: very scarce.

Table 3. Semi-quantitative results of clay minerals in the analysed gneiss samples (percentage of fraction size < 2μm).

	G1	G2	G3	G4	G5	G7	G8	G9	G10	G11
Ilt	100	97.9	100	100	91.7	94.3	94.4	94.3	100	97.1
Sme	-	-	?	?	8.3	?	3.2	?	-	1.9
Kln	-	2.9	-	-	-	5.7	2.4	5.7	-	1.0
Chl	-	-	-	-	-	-	?	-	-	-

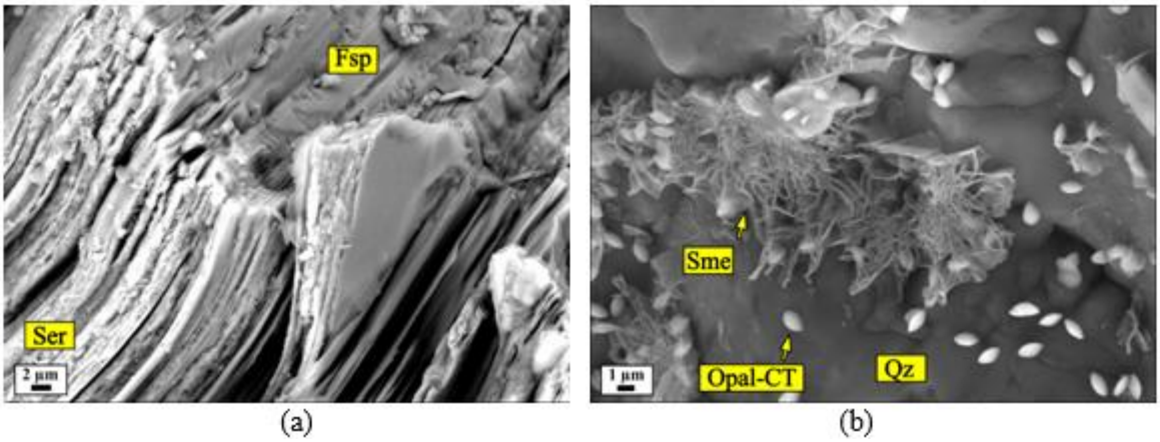

Figure 7. SEM images showing the (a) transformation of feldspar to mica mineral in the process of sericitization at the edges; (b) smectite formations from opal-CT.

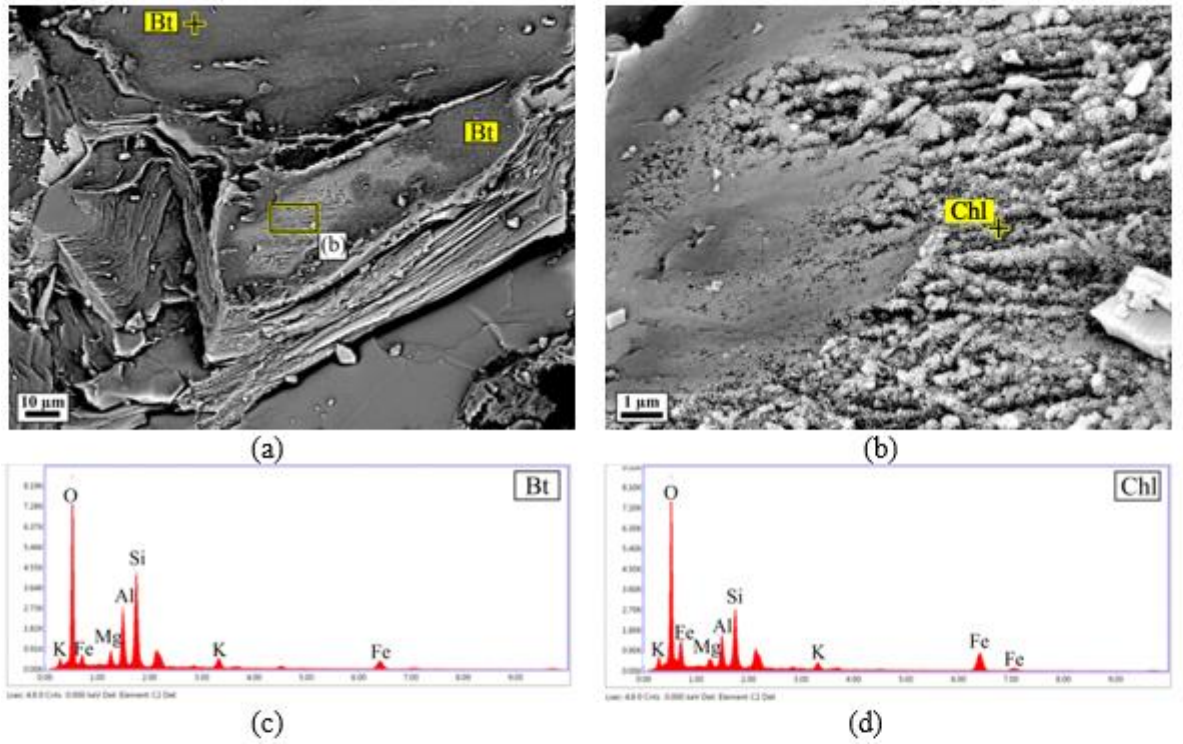

Figure 8. SEM images (Sample G1) showing the (a) elongated biotite mineral; (b) close-up view of the rectangle that points to the rosette-like chlorite formations from biotite; (c) EDX analysis showing the major elements of biotite; (d) EDX analysis showing the major elements of chlorite.

Thin sections which prepared > 63 µm fraction size of the sedimentary rocks point to different features, except all contain sericitization. Coal-underlying samples mainly consist of sedimentary lithic grains, while overlying samples contain mineral grains, mainly quartz and lesser feldspar, with sericitization at their edges. Some samples have bioclast cavities filled with lithic and opaque particles that point to the ostracods [44] (Figure 10). SEM results show that main transformation is kaolinisation from biotite, while serisitation from feldspar is lesser (Figure 11-13).

Major mineral composition of the sedimentary rock samples as detected by XRD analysis were quartz, plagioclase, K-feldspar and mica. The -2 µm fraction of the samples consists of illite, smectite and kaolinite with a minor amount of mixed-layer species. XRD diffractograms of coal-underlying sample, TU-18B, and coal-overlying kaolin rich sample, TU-18A are given in Figure 14. Illite was determined by (001) peak at 10.00-10.20 Å. Smectite was determined by peak at 12.00-14.00 Å, that expanded to 17.00-17.30 Å following ethylene-glycolation; the intensity of this peak collapsed to 10.05-10.21Å following heating at 550^{o}C. Kaolinite was determined from its (001) peak at 7.00-7.20 Å and (002) peak at 3.57 Å, absence of swelling with ethylene-glycol treatment, and those peaks destroyed at 550^{o}C due to dehydroxylation. The contents of main clay minerals were calculated semi-quantitatively according to the XRD determinations of -2 µm fraction for each sample. These results were re-calculated according to the -2 µm particle size amount of whole rock samples, which were analysed via Adreasen pipette method (Figure 15).

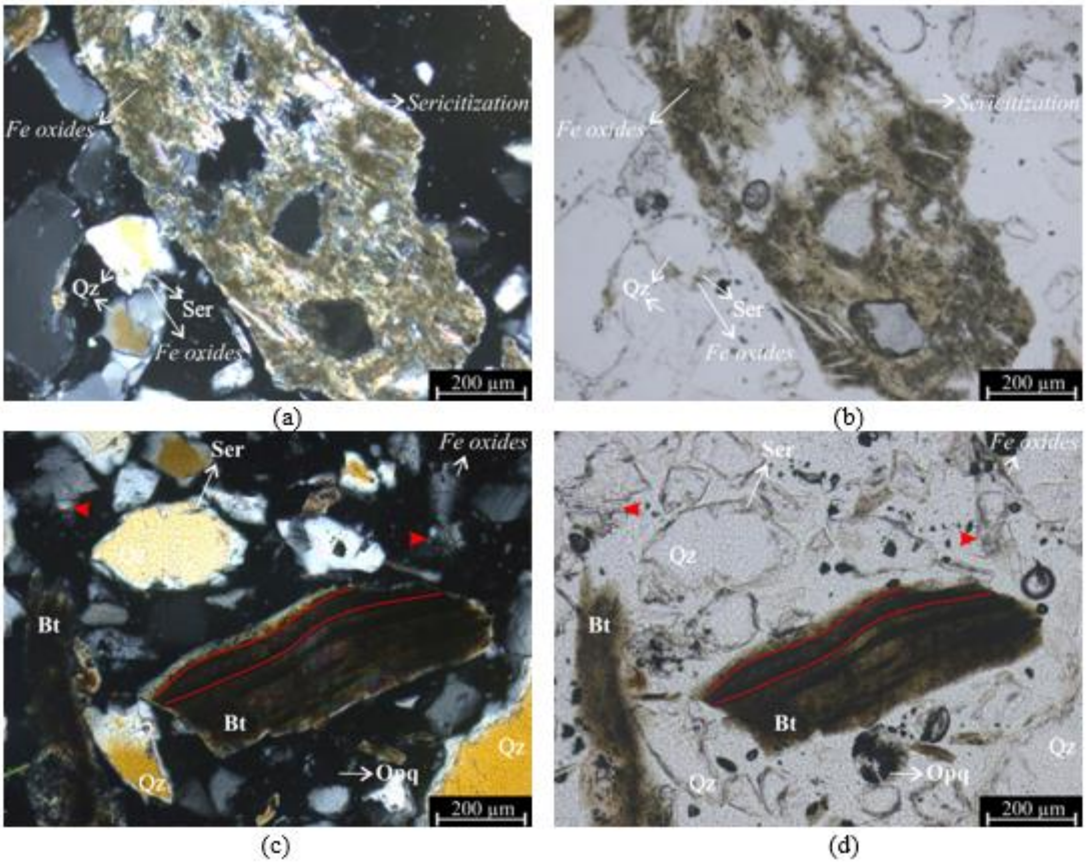

(a) (b) (c) (d)

Figure 9. Photomicrographs of the coal-underlying sedimentary rock samples (fraction size > 63 µm): (a) with crossed polarizers. Sericitization and chloritization in detritic grain; (b) in plane polarized light (TU-1B); (c) with crossed polarizers; (d) in plane polarized light (TU-2B).

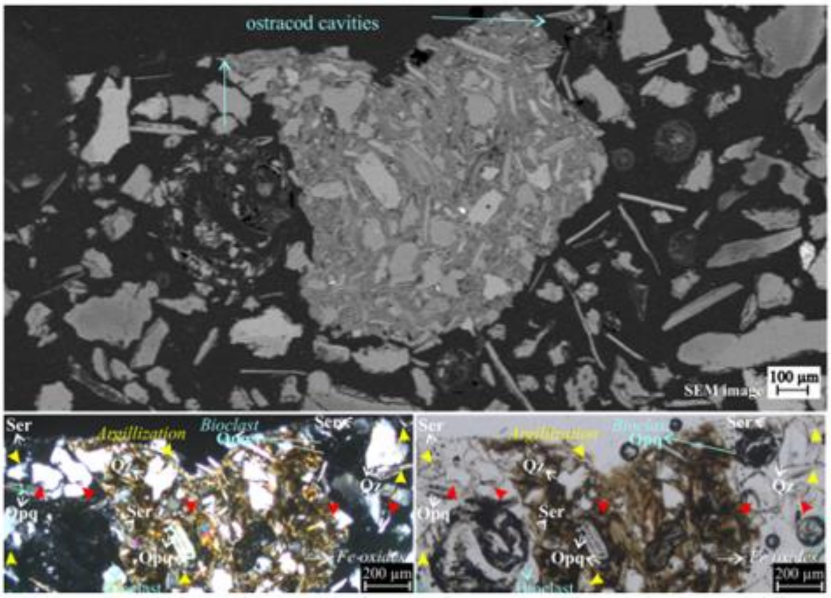

Figure 10. Photomicrographs of the coal-underlying sedimentary rock sample with crossed polarizers and in plane polarized light (TU-2B).

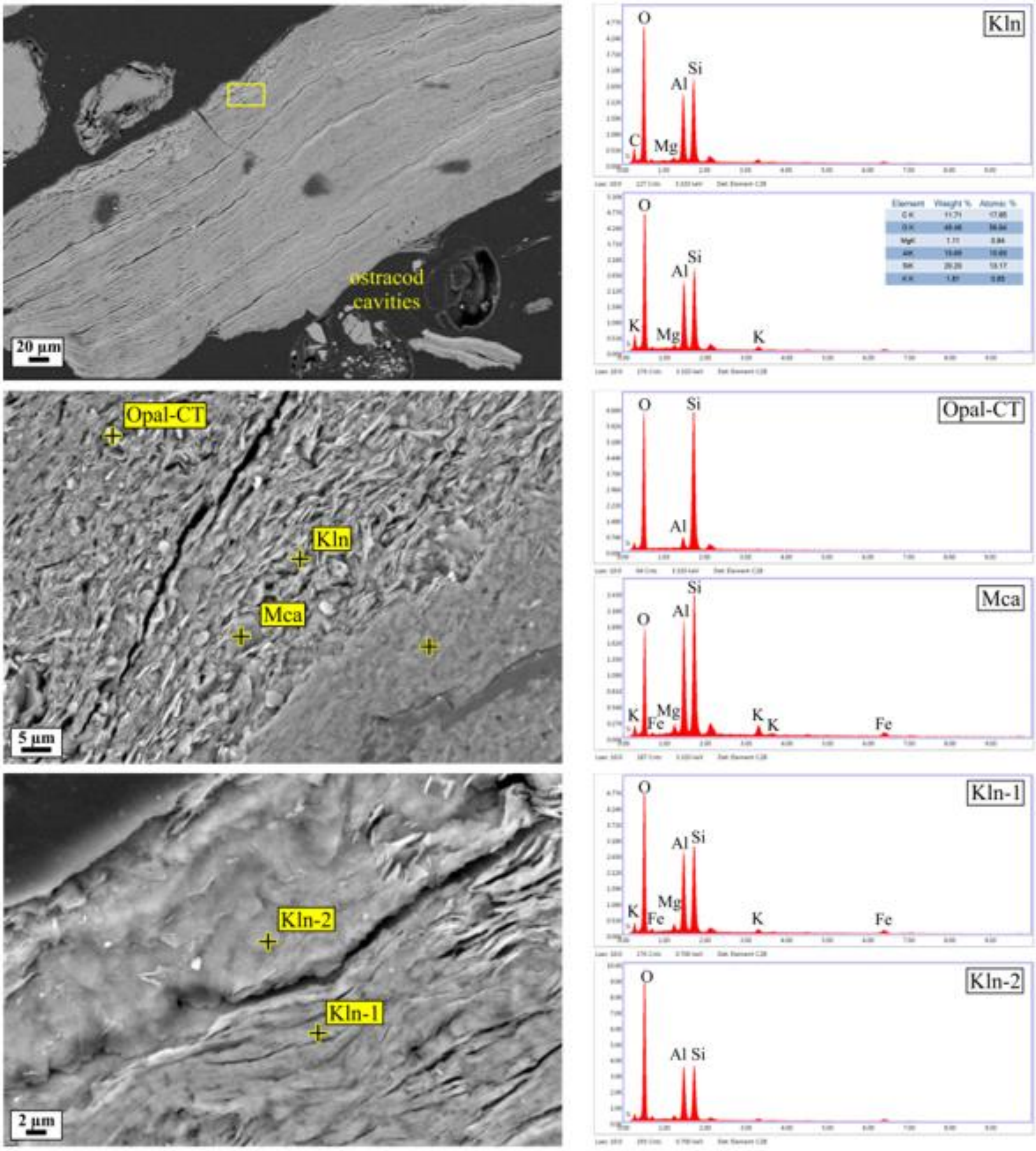

(a) (b)

Figure 11. SEM images (TU-2B) showing the the (a) kaolinisation process of mica mineral; (b) EDX analyses showing the major elements of the selected points. This mica is the same pointed in Figure 9.

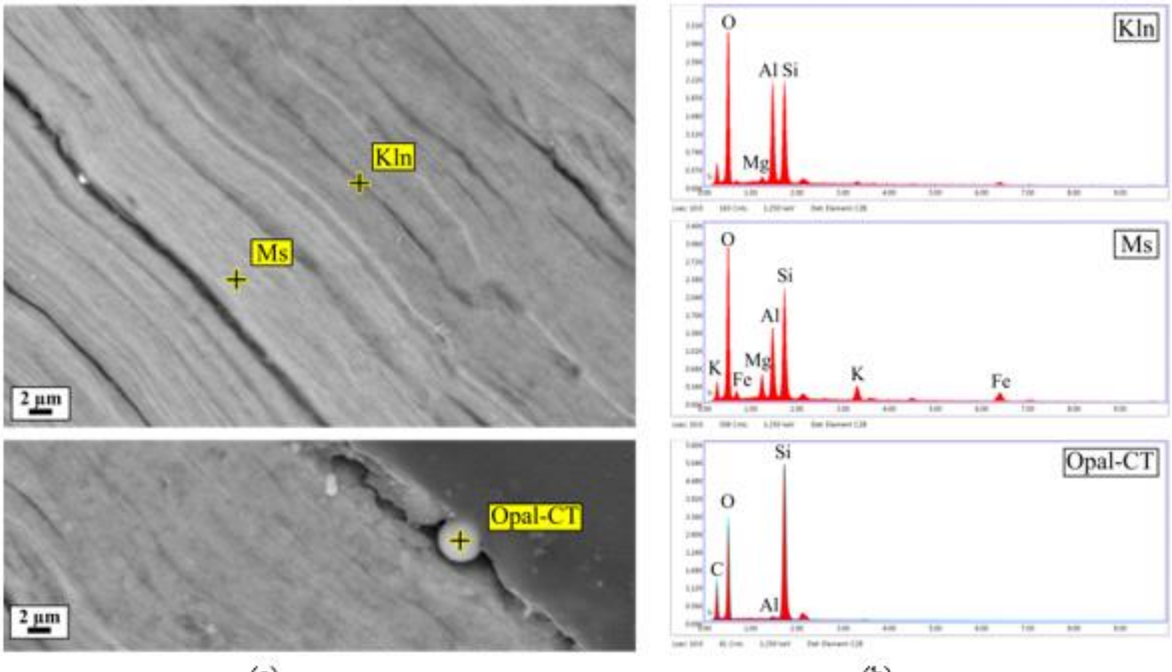

(a) (b)

Figure 12. SEM images (TU-18A) showing the the (a) kaolinisation process of mica mineral; (b) EDX analyses showing the major elements of the selected points.

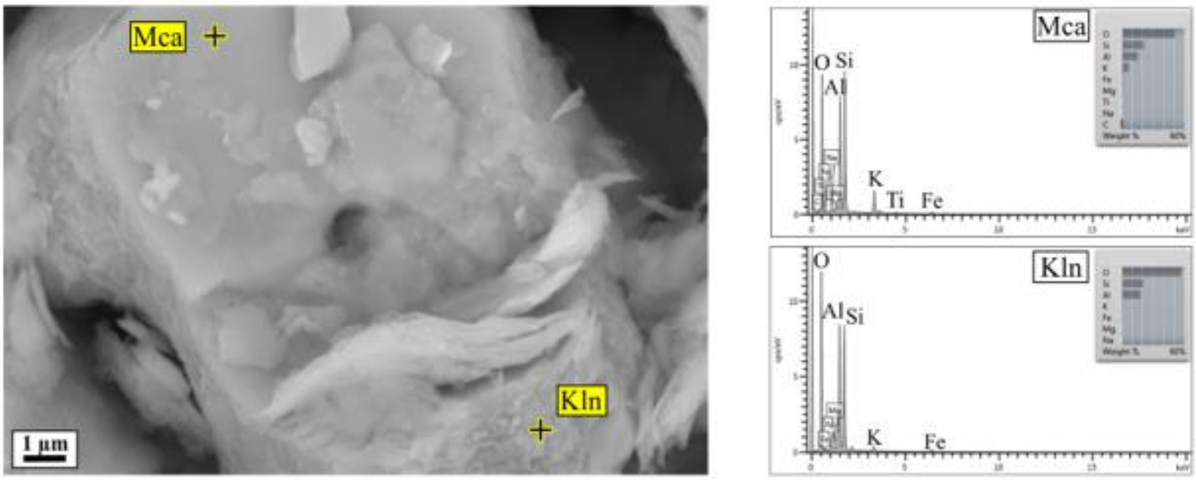

(a) (b)

Figure 13. SEM images (TU-2A) showing the the (a) kaolinisation process; (b) EDX analyses showing the major elements of the selected points.

The formation of micas generally is observed within the zone of slightly changed parent rock and locally in the kaolinite-mica zone. Incongruent dissolution of feldspars in these zones leads to the formation sericite and/or illite on their surface. This process takes place under alkaline conditions with the activity of K^+ ions in the solutions. Local formation of sericite is observed at the borders and along cracks of quartz grains, which is formed probably by dissolution of quartz in solutions containing ions of K^+ and

Al^{3+}, the latter being provided by minerals remaining with them in equilibrium [45]. Furthermore, kaolinite is accompanied by feldspar as well as opal-CT and quartz. This indicates that Al is taken up from feldspar during the in-situ conversion to kaolinite via hydration of feldspar [46-48].

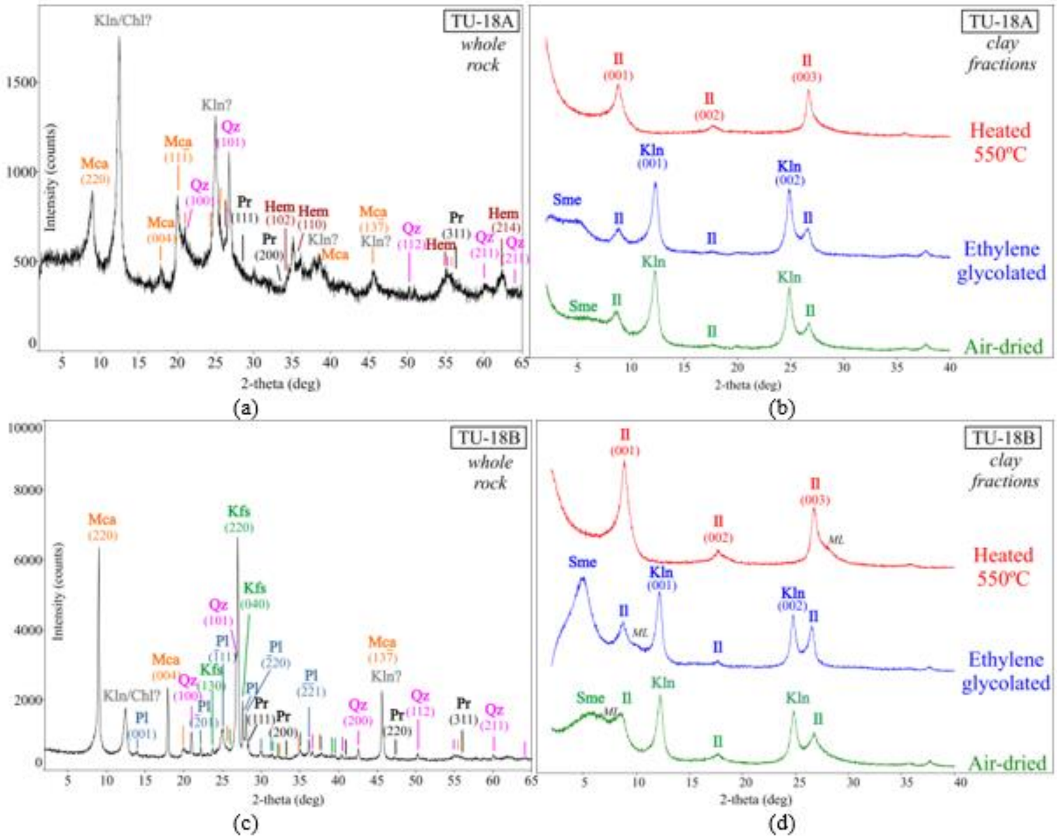

Figure 14. X-Ray diffractograms of the (a) whole rock mineral compositions of coal-overlying sample; (b) clay compositions of -2 µm fraction (TU-18A); (c) whole rock mineral compositions of coal-underlying sample; (d) clay compositions of -2 µm fraction (TU-18B).

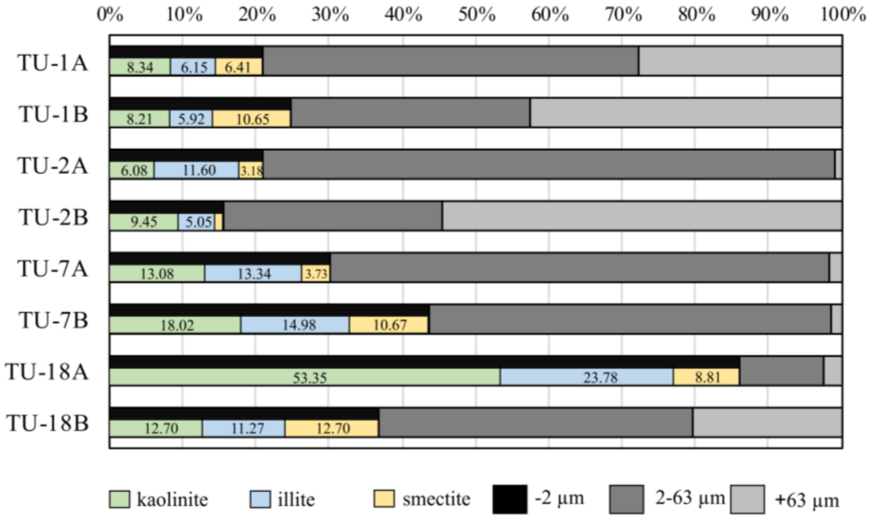

Figure 15. Semi-quantitative results of clay minerals within -2 µm fraction size of the sedimentary rock samples.

4.2. Geochemistry

In order to reveal the main geochemical characteristics of the gneiss samples, classical nomenclature diagrams were applied. The chemical compositions of gneiss and sedimentary rock samples were given in Table 5 and 6, respectively. Orthogneiss samples of study area were consisted of granites [49]. They were classified as calc-alkaline [50, 51] and showed peraluminous composition [52] (Figure 16). Al_2O_3 have negative corelation with SiO_2 element variation with higher amount in coal-underlying samples. The SiO_2/Al_2O_3 is less than two in the samples, that indicates low-maturity of sedimentary rock samples [53] (Figure 17). Chondrite-normalized [54] rare earth element patterns of gneiss and sedimentary rock samples were shown in Figure 18. Negative Eu anomalies of gneiss samples, suggesting the significance of plagioclase fractionation. Sedimentary rock samples also have negative Eu anomalies, suggesting the derivation from these bedrocks. NASC (North American Shale Composite) [55], PAAS Post-Archean Australian Shale) [56], ES (European Shales) [57] and UC (Upper Crust) [58] values are also plotted to the diagram.

Table 5. Major element (wt. %) and REE (Rare earth element) (ppm) concentrations of gneiss samples.

	G1	**G2**	**G3**	**G4**	**G5**	**G8**	**G9**	**G10**
SiO_2	74.80	74.70	74.23	72.62	69.42	75.89	75.54	76.87
Al_2O_3	13.19	13.34	13.57	14.19	17.29	12.58	13.38	13.08
Fe_2O_3	1.42	1.33	1.43	1.79	0.43	1.33	1.37	0.90
MgO	0.36	0.38	0.28	0.49	1.04	0.26	0.68	0.44
CaO	1.17	0.96	0.90	1.27	0.80	0.60	0.58	0.35
Na_2O	2.72	3.19	2.58	2.89	8.76	2.51	4.46	5.33
K_2O	4.92	4.44	5.45	4.76	0.85	4.97	2.20	1.56
TiO_2	0.19	0.20	0.17	0.24	0.23	0.16	0.19	0.11
P_2O_5	0.12	0.11	0.16	0.18	0.25	0.13	0.16	0.18
MnO	0.02	0.02	0.02	0.02	<0.01	0.02	<0.01	<0.01
Cr_2O_3	<0.002	<0.002	<0.002	<0.002	<0.002	<0.002	<0.002	<0.002
LOI	0.80	1.10	1.00	1.30	0.80	1.30	1.20	1.00
Sum	99.78	99.79	99.79	99.76	99.86	99.73	99.81	99.83
CIA[1]	60.00	60.83	60.31	61.40	62.42	60.90	64.89	64.37
La	20.10	16.20	17.60	23.20	1.60	12.30	16.90	6.80
Ce	40.60	33.40	35.00	46.50	2.90	32.50	33.30	15.10
Pr	4.59	3.86	3.98	5.40	0.40	3.20	3.99	1.86
Nd	17.10	14.30	15.00	19.80	1.90	11.30	13.90	6.60
Sm	3.86	3.30	3.53	4.60	0.76	3.00	4.04	1.87
Eu	0.66	0.53	0.51	0.78	0.08	0.37	0.52	0.16
Gd	4.11	3.50	3.77	4.59	0.96	3.24	4.05	1.96
Tb	0.86	0.69	0.80	0.87	0.21	0.75	0.84	0.45
Dy	5.92	4.60	5.52	5.73	1.39	5.67	5.61	3.38
Ho	1.31	1.01	1.22	1.23	0.30	1.29	1.24	0.75
Er	4.00	3.06	3.84	3.64	0.95	4.23	3.77	2.64
Tm	0.58	0.43	0.54	0.52	0.13	0.67	0.58	0.41
Yb	3.57	2.56	3.57	3.12	1.00	4.37	3.60	2.91
Lu	0.51	0.36	0.50	0.44	0.14	0.65	0.53	0.39
Eu/Eu*	0.51	0.48	0.43	0.52	0.29	0.36	0.39	0.26
Ce/Ce*	1.02	1.02	1.01	1.00	0.87	1.25	0.98	1.02

[1] $CIA\ (Chemical\ Index\ of\ Alteration) = 100 \times [Al_2O_3 \div (Al_2O_3 + CaO^* + Na_2O + K_2O)]$

$Eu/Eu^* = Eu_N \sqrt[2]{[(Sm_N) * (Gd_N)]}$, $Ce/Ce^* = \sqrt[2]{[(La_N) * (Pr_N)]}$

Table 6. Major element (wt. %) and REE (Rare earth element) (ppm) concentrations of sedimentary rock samples.

	TU-1A	**TU-1B**	**TU-2A**	**TU-2B**	**TU-7A**	**TU-7B**	**TU-18A**	**TU-18B**
SiO_2	62.68	54.52	47.53	44.07	65.59	69.26	49.03	57.09
Al_2O_3	19.87	20.30	23.01	27.56	17.60	16.72	25.45	22.05
Fe_2O_3	2.90	5.21	9.82	4.46	3.46	2.09	4.76	4.70
MgO	1.08	1.61	1.69	1.26	0.99	0.78	1.36	1.16
CaO	0.82	0.92	0.73	0.57	0.67	0.60	0.49	0.66
Na_2O	1.44	1.65	0.84	0.14	1.76	2.27	0.58	1.23
K_2O	3.89	3.83	4.12	2.21	3.19	3.02	3.83	3.71
TiO_2	0.61	0.77	0.93	0.87	0.62	0.66	0.89	0.82
P_2O_5	0.26	0.09	0.10	0.09	0.07	0.03	0.08	0.08
MnO	0.02	0.02	0.11	0.02	0.01	0.02	0.02	0.02
Cr_2O_3	0.01	0.01	0.01	0.01	0.01	0.01	0.01	0.01
LOI	6.30	10.90	10.90	18.60	5.90	4.40	13.30	8.30
Sum	99.88	99.84	99.84	99.87	99.88	99.89	99.82	99.86
CIA[1]	76.36	75.80	76.03	73.95	80.17	83.86	90.42	79.75
ICV[2]	0.54	0.61	0.69	0.57	0.79	0.47	0.35	0.56
La	37.70	49.90	65.20	67.90	38.00	31.20	72.40	57.20
Ce	82.30	101.60	128.80	144.90	74.20	58.20	149.60	116.00
Pr	8.54	11.59	15.05	14.99	8.98	7.10	16.96	13.42
Nd	31.70	43.30	56.90	52.60	32.60	27.00	63.10	49.50
Sm	6.99	8.92	11.76	10.95	6.95	5.37	14.32	10.86
Eu	1.23	1.56	1.95	2.01	1.26	0.95	2.28	1.85
Gd	6.58	8.44	11.64	10.63	6.87	5.10	14.15	11.10
Tb	1.14	1.38	1.94	1.75	1.19	0.82	2.46	1.90
Dy	7.17	8.31	11.45	10.16	7.39	4.65	15.42	11.49
Ho	1.48	1.69	2.39	2.11	1.55	0.96	3.12	2.21
Er	4.10	4.98	6.96	5.95	4.40	2.79	8.97	6.46
Tm	0.61	0.67	0.95	0.79	0.65	0.40	1.27	0.90
Yb	3.64	4.13	5.83	4.93	3.97	2.45	7.81	5.33
Lu	0.53	0.58	0.83	0.66	0.57	0.40	1.06	0.73
Eu/Eu*	0.55	0.56	0.55	0.56	0.51	0.49	0.57	0.52
Ce/Ce*	1.10	0.97	1.02	0.94	0.99	1.03	1.09	1.01

[1] $CIA\ (Chemical\ Index\ of\ Alteration\ ) = 100 \times [Al_2O_3 \div (Al_2O_3 + CaO^* + Na_2O + K_2O)]$

[2] $ICV\ (Index\ of Compositional\ Variability\ ) = [(Fe_2O_3 + K_2O + Na_2O + CaO + MgO + MnO + TiO_2) \div Al_2O_3]$

$$Eu/Eu^* = Eu_N \sqrt[2]{[(Sm_N) * (Gd_N)]},\ Ce/Ce^* = \sqrt[2]{[(La_N) * (Pr_N)}$$

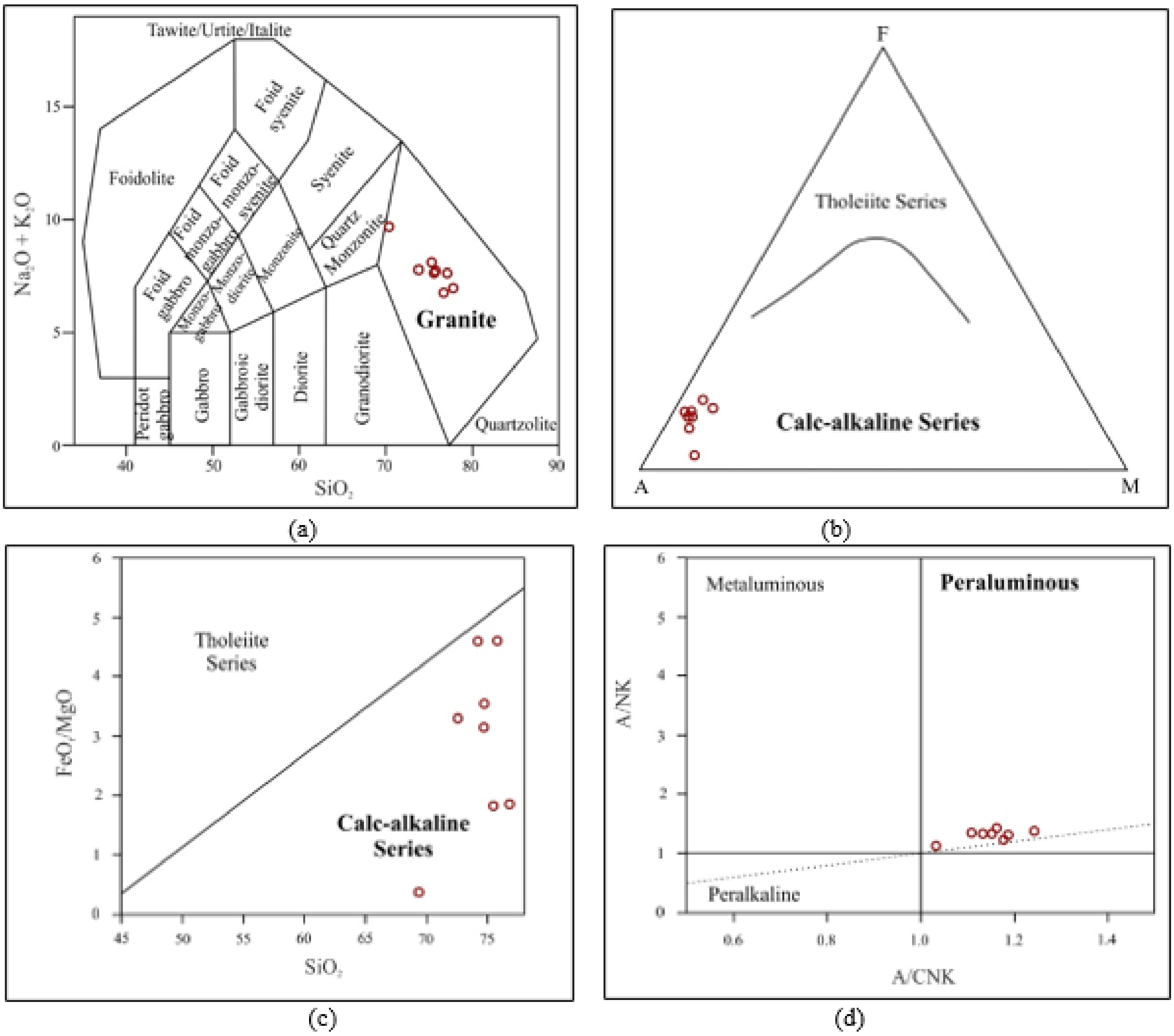

Figure 16. Plotted gneiss samples on (a) SiO_2 vs. (Na_2O + K_2O) binary (TAS) diagram [49]; (b) (Na_2O+K_2O) – FeO_t – MgO (AFM) ternary diagram [50]; (c) SiO_2 vs. FeO_t/MgO binary diagram [51]; (d) Al_2O_3/(CaO+Na_2O+K_2O) vs. Al_2O_3/(Na_2O+K_2O) (mol. %) (A/CNK - A/NK) diagram [52]. (wt% of Fe_2O_3 used in the calculations as FeO_t)

Coal over- and underlying sedimentary rocks plotted to the shale area, accept two samples, which contain coarser detritics (Figure 19 (a)) [59]. In the TiO_2/Ni discrimination diagram sedimentary rock samples plotted to magmatogenic rock field showing felsic to medium trend, whereas in the Sr versus Ba diagram they plotted to the mature field, and/or around mudstone area (Figure 19 (b, c)) [60]. Samples plotted ICV-CIA diagram [61], which pointed to mature field, showing trend from weak to intense weathering (Figure 19(d)). TiO_2-Zr contents of the gneiss points to the felsic igneous rock field, while sedimentary rocks point this area with the samples which has coarser lithology (Figure 19(e)) [62]. Samples plotted to felsic-intermediate igneous provence area in discrimination diagram (Figure 19 (f)) [63]. The coal over- and underlying sedimentary rocks of the study area are about one which change around the limit according to the Ce/Ce* values in a typical shale, which is one [61, 64]. Existing fine –grained framboidal pyrite crystals in the samples shows the anoxic conditions [65].

Gneiss samples and sedimentary rock samples were plotted on A-CN-K (Al_2O_3-CaO*+Na_2O-K_2O) diagram (Figure 20) [66-68]. The initial trend (early weathering) is sub-parallel to the A-CNK boundry of the triangle gneiss samples and their CIA values pointed to slightly weathering. Sedimentary Rock samples CIA values pointed moderately weathering. Studied sedimentary rocks weathering processes and mechanisms have been similar profiles developed from granitoids of diverse composition display systematic, predictable, compositional weathering trends.

Mainly the coal-underlying sedimentary rocks contain detritic particles, which may be related to the metasediments of the basement. Menderes Massif cover series and Karaova Formation of Lycian Nappes contain metasediments: these of Mg-carpholite-bearing rocks and Fe-Mg-carpholite bearing rocks [69], which do not occupy a surface area in Turgut lignite deposit.

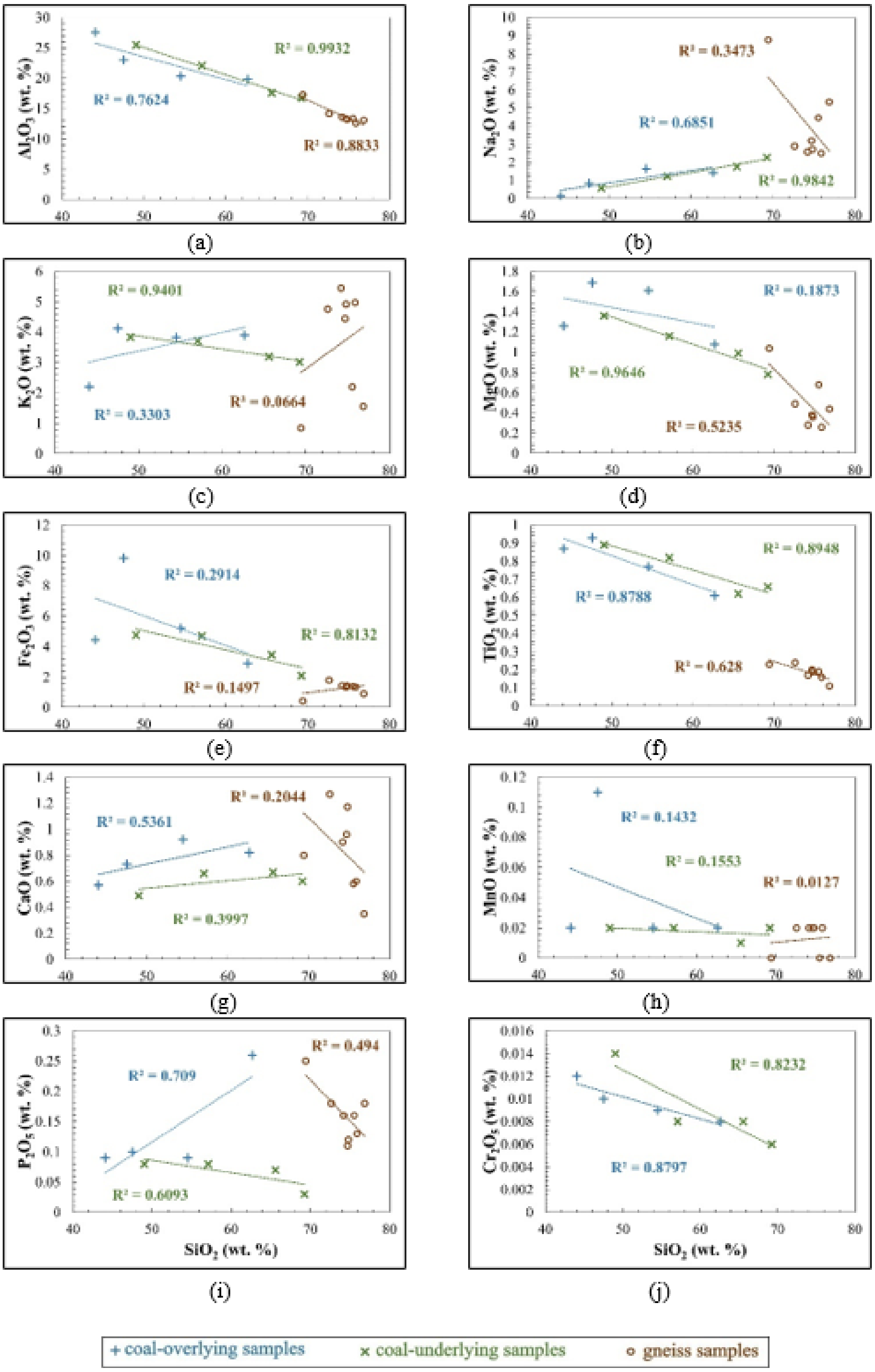

Figure 17. Variation diagrams for (a) Al_2O_3-SiO_2 plot of all samples; (b) Na_2O-SiO_2 plot of all samples; (c) K_2O-SiO_2 plot of all samples; (d) MgO-SiO_2 plot of all samples; (e) Fe_2O_3-SiO_2 plot of all samples; (f) TiO_2-SiO_2 plot of all samples; (g) CaO-SiO_2 plot of all samples; (h) MnO-SiO_2 plot of all samples; (i) P_2O_5-SiO_2 plot of all samples; (j) Cr_2O_5-SiO_2 plot of sedimentary rock samples showing differentiation between concentrations of major oxides.

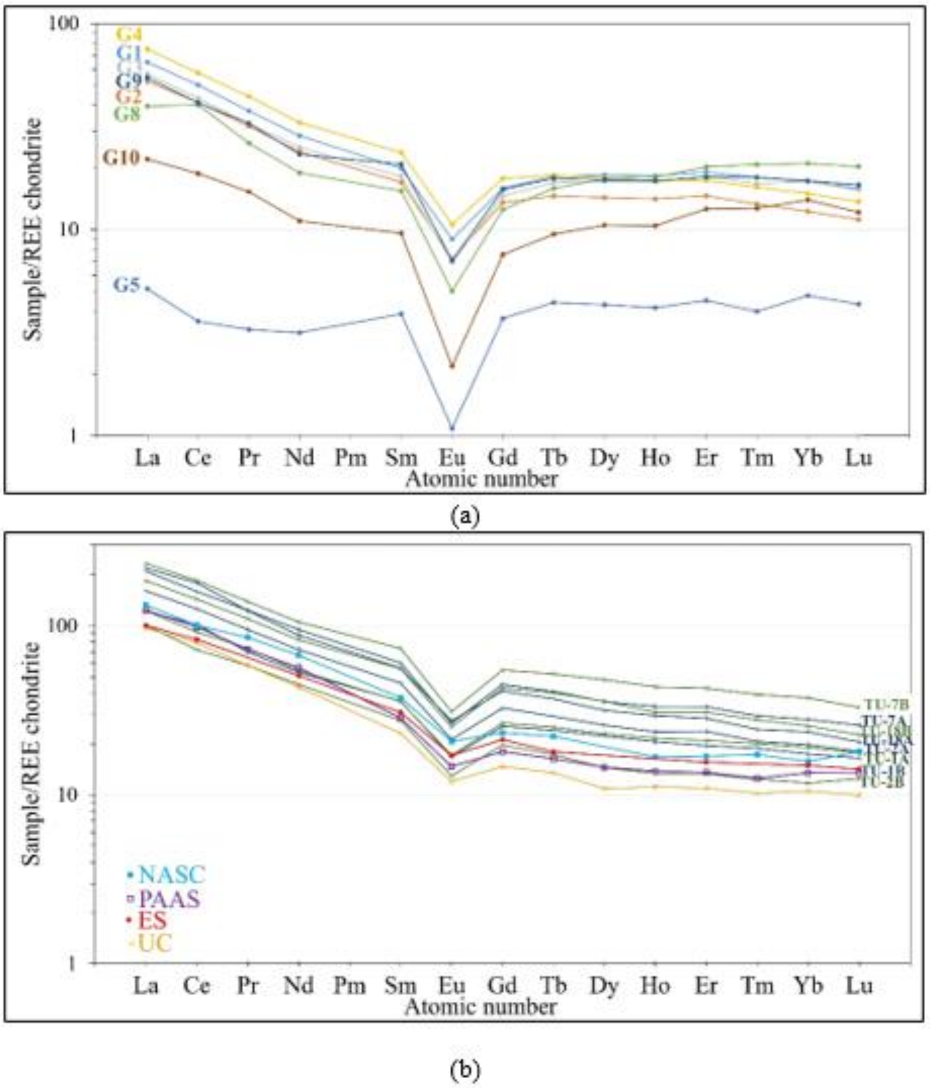

Figure 18. (a) Chondrite – normalized rare earth element (REE) pattern for gneiss samples [54]; (b) Chondrite – normalized rare earth element (REE) pattern for sedimentary rock samples [54]. NASC (North American Shale Composite) [55], PAAS (Post-Archean Australian Shale) [56], ES (European Shales) [57] and UC (Upper Crust) [58] values are plotted for comparison.

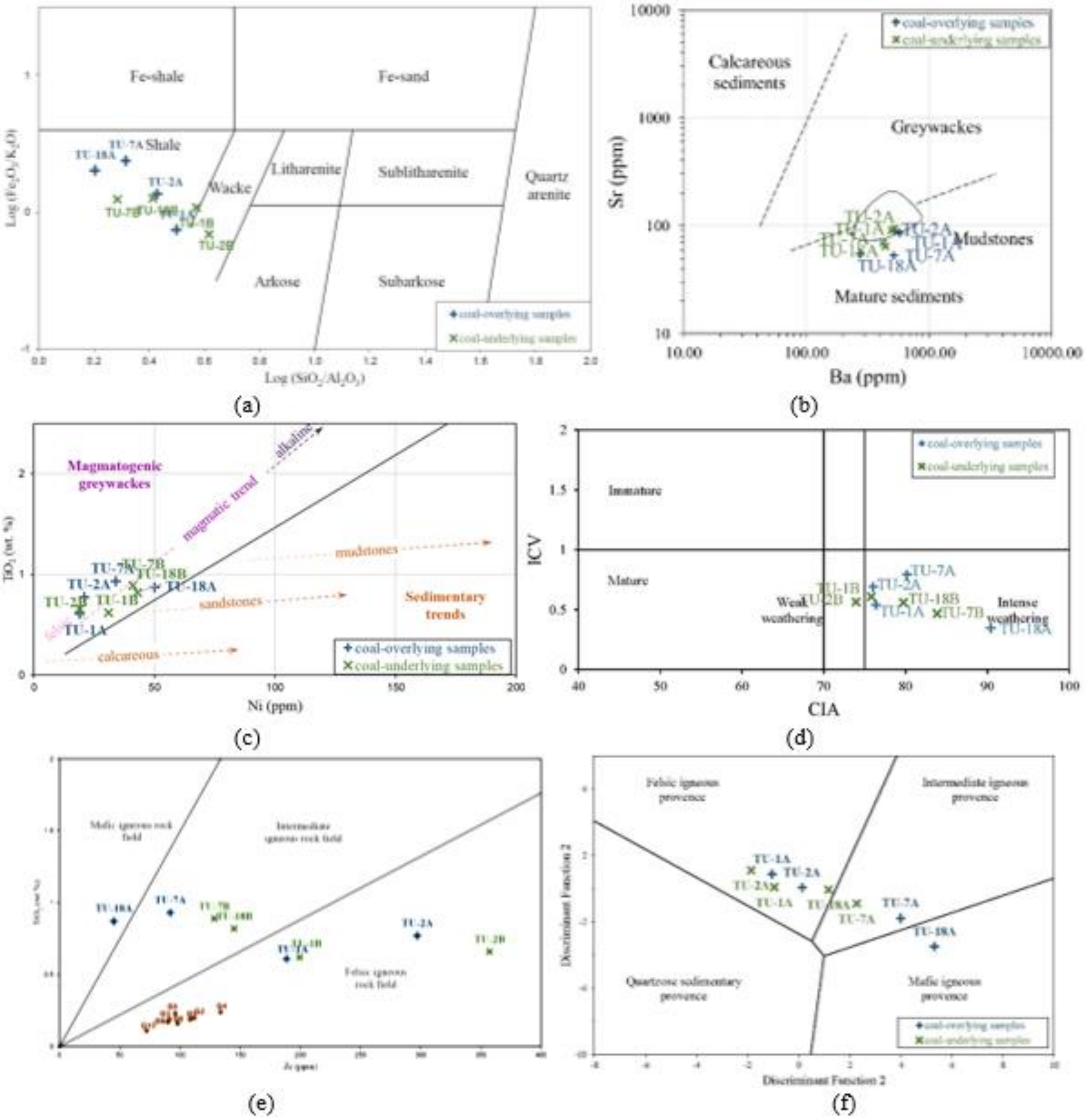

Figure 19. (a) Sand classification diagram [59]; (b) Samples plotted on Sr-Ba diagram showing; (c) TiO_2-Ni plot of sedimentary rock samples showing the magmatogenic greywackes following a trend for asidic rocks [60]; (d) ICV and CIA diagram [61]. (e) TiO_2-Zr contents of the gneiss and sedimentary rock samples [62]; (f) Discriminant plots of sedimentary rock samples [63].

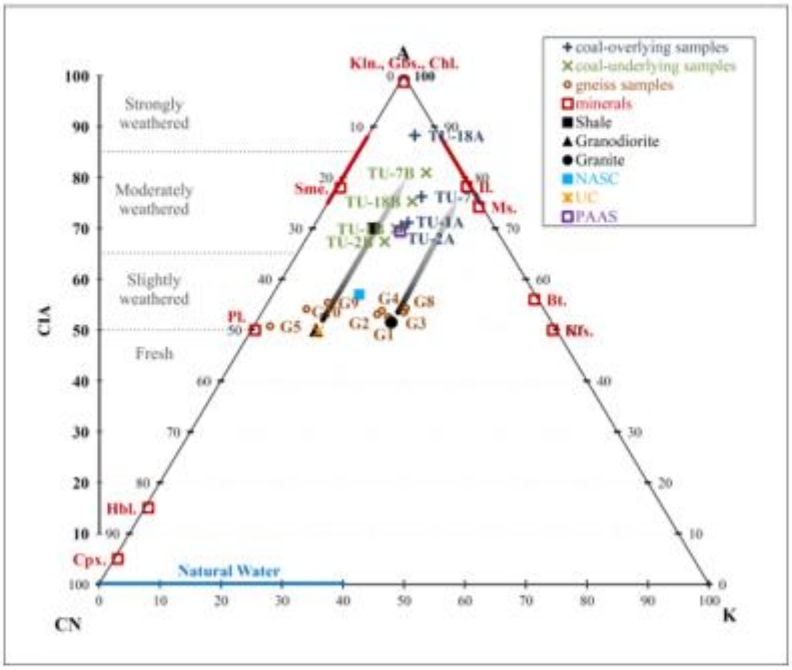

Figure 20. Gneiss and sedimentary rock samples plotted on Al_2O_3-CaO*+Na_2O-K_2O (A-CN-K) diagram (CaO* represents CaO associated with the silicate fraction of the sample.) as molar proportions. Granite, granodiorite, shale, NASC, UC, PAAS samples plotted for comparison as molar proportions of the average values. Red squares are idealized mineral compositions. The arrows are the calculated initial trends followed by the leachates during the initial weathering stages [66-68].

5. CONCLUSION

Dominantly siliciclastic deposits characterize the sedimentary record of the Turgut area (Yatağan Basin). Gneiss samples contain mainly quartz, plagioclase, K-feldspar, muscovite and biotite with a lesser amount of tourmaline, chlorite, garnet, apatite, zoisite, zircon and Fe-oxides. The -2 µm fraction consists mainly of illite, with fewer smectite and kaolinite. Sericitization of feldspar is the main product in gneisses. Coal over-and underlying sedimentary rock samples contain mainly quartz, plagioclase, K-feldspar, muscovite, and biotite with less pyrite and iron oxides. The -2 µm fraction of the sedimentary rock samples consists of variable clay mineral contents. Kaolin content is highly acidic conditions with an opposite correlation to smectite occurrences. The clay mineral content of one sample reaches up to 86%. This sample contains about 53% kaolinite. It is suggested that kaolinite-rich levels must be examined in detail for their utilization potential as raw materials. The geochemistry of Menderes Massif gneisses gave material to the catchment area, whereas the geochemistry of sedimentary rocks is not coherent in all cases. More samples must be studied to understand the weathering effect in the basin.

ACKNOWLEDGEMENTS

This research was supported by Dokuz Eylül University, Department of Scientific Research Projects (BAP) under grant numbers of 2018.KB.FEN.017. The authors are thankful to Dr. İbrahim Gündoğan in memoriam of his valuable discussions and contributions during SEM analysis.

CONFLICT OF INTEREST

The authors stated that there are no conflicts of interest regarding the publication of this article.

AUTHORSHIP CONTRIBUTIONS

Zeynep Büçkün: Formal analysis, Investigation, Writing-original draft, Visualization, Conceptualization. **Mümtaz Çolak:** Supervision, Investigation, Conceptualization.

REFERENCES

[1] McKenzie DP. Active tectonics of the Mediterranean region. Geophys J Roy Astr S 1972; 30: 109-185.

[2] Dumont JF, Uysal S, Şimşek S, Karamanderesi İH ve Letouzey J. Formation of the grabens in southwestern Anatolia. Bull Min Res Expl Inst Turkey 1979; 92: 7-18.

[3] Angelier J, Dumont JF, Karamanderesi İH, Poisson A, Şimşek S, Uysal S. Analysis of fault mechanisms and expansion of southwestern Anatolia since the late Miocene. Tectonophysics 1981; 75: 1-9.

[4] Şengör AMC, Görür N, Şaroğlu F. Strike-slip faulting and related basin formation in zone of tectonic escape: Turkey as a case study. In: Biddle K, Christie-Blick N, editors. Strike-slip deformation, basin formation and sedimentation. SEPM 1985; 227-264.

[5] Barka AA. The North Anatolian Fault zone. Annales Tectonicae 1992; 6: 164-165.

[6] Becker A. An attempt to define a "neotectonic period" for central and northern Europe. Int J Earth Sci 1993; 82-1: 67-83.

[7] Cohen HA, Dart CJ, Akyüz HS, Barka AA. Syn-rift sedimentation and structural development of the Gediz and Büyük Menderes graben, western Turkey. J Geol Soc London 1995; 152: 629-638.

[8] Yılmaz Y, Genç SC, Gürer OF, Bozcu M, Yılmaz K, Karacık Z, Altunkaynak Ş, Elmas A. When did the western Anatolian grabens begin to develop?. Geol Soc Spec Publ 2000; 173: 353-384.

[9] Bozkurt E. Neotectonics of Turkey-a synthesis. Geodin Acta 2001; 14: 3-30.

[10] Bozkurt E. Origin of NE-trending basins in western Turkey. Geodin Acta 2003; 16: 61-81.

[11] Collins AS, Robertson AHF. Kinematic evidence for late Mesozoic-Miocene emplacement of the Lycian Allochthon over the Western Anatolian belt, SW Turkey. Geol J 2003; 38: 107-138.

[12] Bozkurt E, Sözbilir H. Tectonic evolution of the Gediz Graben: field evidence for an episodic, two-stage extension in western Turkey. Geol Mag 2004; 141: 63-79.

[13] Çiftçi NB, Bozkurt E. Folding of the Gediz Graben fill, SW Turkey: extensional and/or contractional origin?. Geod Acta 2008; 21: 145-167.

[14] Sözbilir H, Sarı B, Uzel B, Sümer Ö, Akkiraz S. Tectonic implications of transtensional supradetachment basin development in an extension-parallel transfer zone: The Kocaçay Basin, western Anatolia, Turkey. Basin Res 2011; 23: 423-448.

[15] Atalay Z. Stratigraphy of continental Neogene in the region of Muğla-Yatağan, Turkey. Türkiye Jeol Bül 1980; 23: 93-99.

[16] Hakyemez HY, Örçen S. Sedimentological and biostratigraphical study of the Cenozoic sedimentary rocks between Muğla-Denizli (SW Anatolia). MTA Ankara 1982; Report 7311.

[17] Hakyemez HY. Geology and stratigraphy of the Cainozoic sedimentary rocks in the Kale-Kurbalık area, Denizli, southwestern Turkey. Min Res Expl Bull 1989; 109, 1-14.

[18] Göktaş F. Stratigraphy, sedimentology and regional correlation of Neogene sedimentation surrounding Mugla (GB Anatolia). MTA Ankara 1998; Report 10225.

[19] Akgün F, Sözbilir H. A palynostratigraphic approach to the SW Anatolian molasse basin: Kale-Tavas molasse and Denizli Molasse. Geodin Acta 2001; 14: 71-93.

[20] Becker-Platen JD, Bering A. Lignite study of Yatağan (Muğla) field. MTA Ankara 1966; Report 5995.

[21] Gökmen V. Geology, boreholes and results of lignite deposits in Yatağan-Eskihisar region of Muğla. Doktora Tezi, İstanbul University, İstanbul, Türkiye, 1980.

[22] Ünal D. Geological report of Muğla-Yatağan-Turgut lignite sector. MTA İzmir 1986.

[23] Ünal D. Determination of the reserves and quality of lignite in Muğla-Yatağan-Turgut fields. GELİ 1991.

[24] Graciansky P. Precisions of the metamorphism of the Menderes Massif along its southern edge (SW of Turkey). MTA Derg 1965; 64: 8-22.

[25] Dora OÖ, Kun N ve Candan O. Metavolcanics (leptites) in the Menderes Massif: a possible paleoarc volcanism. METU J Pure Appl Sci 1988; 21 1-2: 413-445.

[26] Dora OÖ, Candan O, Kaya O, Koralay E, Dürr S. Revision of the so-called "leptitegneisses" in the Menderes Massif: A supracrustal metasedimentary origin. Int J Earth Sci 2001; 89-4: 836-851.

[27] Özer S, Sözbilir H, Özkar I, Toker V, Sarı B. Stratigraphy of Upper Cretaceous-Palaeogene sequences in the southern and eastern Menderes Massif (Western Turkey). Int J Earth Sci 2001; 89-4: 852-866.

[28] Candan O, Dora ÖO, Oberhänslı R, Koralay E, Çetinkaplan M, Akal C, Satır M, Chen F, Kaya O. Stratigraphy of the Pan-African basement of Menderes Massif and its relationship to the Late Neoproterozoic/Cambrian evolution of Gondwana. MTA Derg 2011; 142: 25-68.

[29] Candan O, Oberhänsli R, Dora ÖO, Çetinkaplan M, Koralay E, Rimmelé G, Chen F, Akal C. Polymetamorphic evolution of the Pan-African Basement and Paleozoic-Early Tertiary cover series. MTA Derg 2011; 142: 123-165.

[30] Koralay EO, Candan O, Akal C, Dora OÖ, Chen F, Satır M, Oberhänslı R. The geology and geochronology of the Pan-African and Triassic metagranitoids in the Menderes Massif, Western Anatolia, Turkey. Bull Min Res Expl Inst 2011; 142: 69-119.

[31] Nebert K. Report on the geology of the centre of Denizli-Acıgöl and geological maps made within the 1:100,000 scale Denizli 105/1, 105/2, Isparta 106/1. MTA Ankara 1956; Report 2509.

[32] Abdüsselamoğlu MŞ. Report on the correlation of geological formations surrounding Muğla-Yatağan. MTA Ankara 1965; Report 3497.

[33] Başarır E. Geology and petrography of the Southern Margin of the Menderes Massif to the East of Lake Bafa. Ege Uni Sci Fac 1970; 102: 1-44.

[34] Becker-Platen JD. Lithostratigraphische Untersushungen im Kanozoikum Südwest-Anatoliens (Türkei) (Kanozoikumund Braunkohlen der Türkei, 2). Beih Geol Jb 1970; 97: 144.

[35] Gökten E, Havzaoğlu T, Şan Ö. Tertiary evolution of the central Menderes Massif based on structural evolution of metamorphics and sedimentary rocks between Salihli and Kiraz (western Turkey). Int J Earth Sci 2001; 89: 745-756.

[36] NASA Earth Data. ESDS Program 2022: https://urs.earthdata.nasa.gov/

[37] 30-Meter SRTM Tile Downloader 2022: https://dwtkns.com/strm30m/

[38] Brown G, Brindley GW. X-Ray diffraction procedures for clay mineral identification. In: Brindley GW, Brown G, editors. Crystal Structures of Clay Minerals and their X-Ray Identification. London, Great Britain: Spottiswoode Ballantyne Ltd, 1980. pp. 305-359.

[39] DIN 66115 (Deutsche Institute fürNormunge. V.). Partikelgrößenanalyse; Sedimentationsanalyse im Schwerefeld; Pipette-Verfahren, Germany, 1983-02.

[40] Whitney DL, Evans BW. Abbreviations for names of rock-forming minerals. Unraveling the effects of potassium metasomatism in sedimentary rocks and paleosols, with implications in weathering conditions and provenance. Am Min 2010; 95: 185-187.

[41] Warr LN. Recommended abbreviations for the names of clay minerals and associated phases. Clay Miner 2020; 55: 261-264.

[42] Bozkurt E, Winchester AJ, Mittwede S, Ottley C. Geochemistry and tectonic implications of leucogranites and tourmalines of the southern Menderes Massif, southwest Turkey. Geodin Acta 2006;19/5: 363–390.

[43] Candan O, Koralay OE, Akal C, Kaya O, Oberhänslı R, Dora OÖ, Konak N, Chen F. Supra-Pan_African unconformity between core and cover series of the Menderes Massif/Turkey and its geological implications. Precambrian Res 2011; 184:1-23.

[44] Yılmaz Ö, Güngör T, Kayseri-Özer MS, Akgün F, Mayda S, Kaya T, Nazik A, Büyükmeriç Y. Stratigraphy of the Mio-Pleistocene sequence in Göktepe region based on the fossil record (Muğla, SW Turkey). Turk J Earth Sci 2020; 29: 501-520.

[45] Stoch L, Sikora W. Transformations of micas in the process of kaolinitization of granites and gneisses. Clay Clay Miner 1976; 24: 156-162.

[46] Hemley JJ, Jones WR. Chemical aspects of hydrothermal alteration with emphasis on hydrogen metasomatism. Economic Geol 1964; 59: 538-569.

[47] Macaulay CI, Fallick AE, Haszeldine RS. Textural and isotopic variations in diagenetic kaolinite from the Magnus oilfield sandstones. Clay Minerals 1993; 28: 625-639.

[48] Kadir S, Karakaş Z. Mineralogy, chemistry and origin of halloysite, kaolinite and smectite from Miocene ignimbirites, Konya, Turkey. N Jb Miner Abh 2002; 177-2: 113-132.

[49] Middlemost EAK. Naming materials in magma/igneous rock system. Earth Sci Rev 1994; 37: 215-224.

[50] Irvine TN, Baragar WRA. A guide to the chemical classification of the common volcanic rocks. Can J Earth Sci 1971; 8: 523–548.

[51] Miyashiro A. Volcanic rock series in island arcs and active continental margins. Am J Sci 1974; 274: 321–355.

[52] Shand SJ. Eruptive Rocks. Their Genesis, Composition, Classification, and Their Relation to Ore-Deposits with a Chapter on Meteorite. New York: John Wiley & Sons 1943.

[53] Roser BP, Cooper RA, Nathan S, Tulloch AJ. Reconnaissance sandstone geochemistry, provenance, and tectonic setting of the lower Paleozoic terranes of the West Coast and Nelson, New Zeland. N Z J Geol Geophys 1996; 39: 1-16.

[54] Boynton WV. Geochemistry of the Rare Earth Elements: Meteorite Studies. In: Henderson P, editor. Rare Earth Element Geochemistry. Elsevier 1984. pp. 63-114.

[55] Gromet LP, Dymek RF, Haskin LA, Korotev RL. The "North American shale composite": Its compilation, major and trace element characteristics. Geochim Cosmochim Acta 1984; 48: 2469-2482.

[56] Taylor SR, Mclennan SM. The Significance of the rare earths in geochemistry and cosmochemistry. In: Gschneidner KA, Eyrin L, editors. Handbook on the Physics and Chemistry of Rare Earths. Elsevier Science Publishers 1988; 11. pp. 485-578.

[57] Haskin MA, Haskin LA. Rare earths in European Shales: a redetermination. Science 1966; 154: 507-509.

[58] Taylor SR, Mclennan SM. The comparison and evolution of the continental crust: rare earth element evidence from sedimentary rocks. Phil Trans R Soc Lond A 1981; 301, 381-399.

[59] Herron MM. Geochemical classification of terrigenous sands and shales from core or log data. J Sediment Petrol 1988; 58: 820-829.

[60] Floyd PA, Winchester JA, Park RG. Geochemistry and tectonic setting of Lewisian clastic metasediments from the Early Proterozoic Loch Maree Group of Gairloch, NW Scotland. Precambrian Res 1989; 45, 203-214.

[61] Cox R, Lowe DR, Cullers RL. The influence of sediment recycling and basement composition on evolution of mudrock chemistry in the southwestern United States. Geochim et Cosmochim Acta 1995; 59-14: 2919-2940.

[62] Hayashi KI, Fujisawa H, Holland HD, Ohmoto H. Geochemistry of ~1.9 Ga sedimentary rocks from norteastern Labrador, Canada. Geochim Cosmochim Acta 1997; 61: 4115-4137.

[63] Roser BP, Korsch. Provenance signatures of sandstone-mudstone suites determined using discriminant function analysis of major-element data. Chem Geol 1988; 67: 119-139.

[64] Cullers RL, Berendsen P. The provenance and chemical variation of sandstones associated with the Mid-Continent Rift system, USA. Eur J Mineral 1998; 10: 987-1002.

[65] Büçkün Z, Çolak M. Petrological, mineralogical and geochemical proxies to the organic matter dispersed in the sedimentary rocks in Turgut area, Yatağan Basin, SW Türkiye. Bull Geol Soc Greece Sp Publ (BGSG) 2023; 12: 48.

[66] Nesbitt HW, Young GM. Formation and diagenesis of weathering profiles. J Geol 1989; 97: 129-147.

[67] McLennan SM, Hemming S, McDaniel DK, Hanson GN. Geochemical approaches to sedimentation, provenance and tectonics. Geol Soc Am Spec Pub 1993; 284: 21-40.

[68] Fedo CM, Nesbitt HW, Young GM. Unraveling the effects of potassium metasomatism in sedimentary rocks and paleosols, with implications in weathering conditions and provenance. Geology 1995; 23: 921-924.

[69] Rimmelé G, Parra T, Goffé B, Oberhänslı R, Candan O. Exhumation paths of high pressure-low-temperature metamorphic rocks from the Lycian Nappes and the Menderes Massif (SW Turkey): a Multi-equilibrium approach. J Petrol 2005; 46: 641-669.